

# UC Davis

## UC Davis Previously Published Works

### Title

Enhanced adsorption/extraction of bisphenols by pyrrolic N-based 3D magnetic carbon nanocomposites for effervescence-assisted solid-phase microextraction of bisphenols from juices and the underlying interaction mechanisms

### Permalink

<https://escholarship.org/uc/item/9kh4w4dk>

### Authors

Liu, Tingting  
Wang, Qi  
Kong, Jia  
et al.

### Publication Date

2022-11-01

### DOI

10.1016/j.cej.2022.137690

Peer reviewed



# Enhanced adsorption/extraction of bisphenols by pyrrolic N-based 3D magnetic carbon nanocomposites for effervescence-assisted solid-phase microextraction of bisphenols from juices and the underlying interaction mechanisms

Tingting Liu<sup>a</sup>, Qi Wang<sup>a</sup>, Jia Kong<sup>a</sup>, Lei Zhang<sup>a</sup>, Feiyue Qian<sup>a</sup>, Ming Gao<sup>a</sup>, Yongli Ding<sup>a</sup>, Randy A. Dahlgren<sup>b</sup>, Xuedong Wang<sup>a,\*</sup>

<sup>a</sup> Jiangsu Key Laboratory of Environmental Science and Engineering, School of Environmental Science and Engineering, Suzhou University of Science and Technology, Suzhou 215009, China

<sup>b</sup> Department of Land, Air and Water Resources, University of California, Davis, CA 95616, USA

## ARTICLE INFO

### Keywords:

CoNi-N-CNTs/rGO 3D nanocomposite  
Pyrrolic N  
Effervescence tablet-assisted magnetic solid-phase microextraction  
Bisphenols  
DFT theoretical calculation

## ABSTRACT

Herein, we fabricated a magnetic 3D nanocomposite based on Co,Ni-codoped and N-modified carbon nanotubes and reduced graphene (CoNi-N-CNTs/rGO). This nanomaterial possessed strong magnetism due to the presence of Co-Ni alloy, abundant defect sites owing to N doping, and a 3D multi-porous structure resulting from CNT *in-situ* growth on the graphene surface. Based on DFT calculations, H-bonding, hydrophobic and  $\pi$ - $\pi$  conjugation were inferred to facilitate bisphenol adsorption by nanocomposites, among which  $\pi$ - $\pi$  interactions provided the greatest adsorption contribution within a given N-doping type. By employing BPM as model compound, the adsorption energies ( $\Delta E_a$ ) for  $\pi$ - $\pi$  conjugation were  $-1.80$ ,  $-1.59$  and  $-2.08$  eV for graphitic-N, pyridinic-N, and pyrrolic-N, respectively. This infers that pyrrolic-N sites form the strongest BP sorption bonds with the nanocomposite. The nanocomposites were utilized as an extractant in an effervescence tablet-assisted magnetic solid-phase microextraction (ET-MSPE) procedure that was optimized using Plackett-Burman design (PBD) and central composite design (CCD). Under optimized conditions, the ET-MSPE/HPLC-FLD method provided strong analytical performance for quantification of six BPs in juice with limits of detection of  $0.06$ – $0.20$   $\mu\text{g/L}$ , recoveries of  $82.4$ – $103.7$  % and RSDs of  $1.2$ – $5.3$  %. The particular novelty of this study lies in demonstrating the enhancement of adsorption/extraction efficiencies for BPs by nanocomposites resulting from N doping to generate the superior adsorption properties associated with the pyrrolic-N structure. These findings provide a theoretical foundation to inform the rational design of N-doped adsorbents/extractants based on a rigorous understanding of the molecular interactions occurring between carbon-based nanocomposites and BP analogues.

## 1. Introduction

Bisphenols (BPs) are one of the most widely produced chemicals worldwide for use in the production of plastics, flame retardants, antioxidants, and other fine chemical products [1]. BPs are ubiquitous within the environment and are readily absorbed by the human body. Human-health consequences include endocrine disrupting effects and increased risk of breast, ovarian, and testicular cancer [2,3]. BPs have been detected in many environments and food media in the range of  $14$ – $521$  ng/mL (or ng/kg)[4–6]. Owing to human-health concerns, the European Commission (2017) decreased the maximum residual limit of

bisphenol A (BPA) in food matrices from  $0.60$  to  $0.05$  mg/kg [7]. In China, the maximum BP concentration in food contact materials is  $< 0.60$  mg/kg [8].

To date, several analytical approaches have been reported for BP quantification, such as solid-phase microextraction (SPME) [10], dispersive liquid–liquid microextraction (DLLME) [9,11], and effervescent tablet-assisted dispersive solid-phase microextraction (ET-DSM) [8,12,13]. The ET-DSM method incorporating an effervescent reaction, as pioneered by Lasarte-Aragones and coworkers, is often a preferred method owing to its convenient operation and remote/outdoor feasibility [13]. Specifically, the extraction solvent or solid extractant/

\* Corresponding author at: School of Environmental Science and Engineering, Suzhou University of Science and Technology, Suzhou 215009, China.  
E-mail address: [zjuwxd@163.com](mailto:zjuwxd@163.com) (X. Wang).

adsorbent is dispersed into the solvent by CO<sub>2</sub> bubbles produced by reaction of acid and alkaline sources introduced into the sample. The effervescent mixing increases contact between the extractant and aqueous phase, thereby enhancing the extraction efficiency. Additionally, the ET-DSM method integrates with magnetic recovery to construct the ET-MSPE procedure, which employs an external magnet to separate adsorbent/extractant after extraction to avoid extra steps such as centrifugation, further improving the efficiency of sample pretreatment. Given its operational efficiencies, ET-MSPE approaches have rapidly developed for the detection of trace pollutants, including pesticides [14,15], polycyclic aromatic hydrocarbons (PAHs) [16,17], and BPs [8,12].

The development of ET-MSPE approaches closely relies on innovation of adsorbents/extractants, and the increasing development of novel nanomaterials provides a broad array of adsorbent choices. Many types of nanomaterials have been employed in the pretreatment steps for food and environmental sample analyses [18,19], including carbon nanomaterials [20], metal organic frameworks (MOFs) [21], covalent organic frameworks (COFs) [22], and molecularly imprinted polymers [23]. Among these nanomaterials, carbon nanotubes (CNTs) and reduced graphene (rGO) have excellent mechanical, optical and electrochemical properties, resulting in their widespread utilization in the adsorption and removal of pollutants [20,24]. Magnetization of carbon materials is an important means of preparing magnetic adsorbent/extractant in ET-MSPE technology. In the magnetization process, the commonly used magnetic nuclei are mainly focused on Fe, Co, Ni and their compounds, such as Fe<sub>3</sub>O<sub>4</sub>,  $\gamma$ -Fe<sub>2</sub>O<sub>3</sub>, MFe<sub>2</sub>O<sub>4</sub> (M = Fe, Co, Ni, Cu and Zn), Fe<sub>3</sub>S<sub>4</sub>, etc. Surface modification of carbon materials is often carried out by co-precipitation, hydrothermal synthesis and sol-gel approaches. The modification process involved often requires a stepwise experiment, and the magnetic cores are prone to agglomerate or fall off during the composite process, which restricts the development of magnetic adsorption/extraction materials to a certain extent. Hao and colleagues successfully prepared magnetic nanoporous carbon material (MNC) by one-step carbonization of ZIF-67 formed from cobalt salt and dimethylimidazole [46]. The prepared Co-MNPC has strong magnetism due to the formation of Co nanoparticles in the carbonization process, and the Co is wrapped in the carbon material, thus protecting the magnetic stability of the material and simplifying the magnetization process. It provides new insights into the development of simple and efficient magnetic carbon nanosorption/extraction materials. Compared to Co, Ni monomer, Co-Ni alloy has higher magnetic anisotropy, stronger magnetic susceptibility and greater magnetic coercivity. In contrast with Fe<sub>3</sub>O<sub>4</sub> and other compounds, Co-Ni alloy does not need to be prepared in advance, and it only needs to mix Co source, Ni source and carbon source and nitrogen source evenly, freeze dry fixation, and then carbonization can be formed and wrapped in carbon material, which further solves the problem of magnetic core agglomeration and falling off. Synthesizing the above information, Co-Ni alloy nanomaterial has a great application potential in the ET-MSPE method.

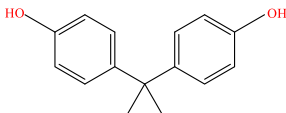
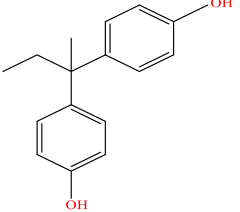
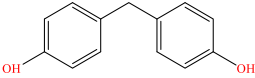
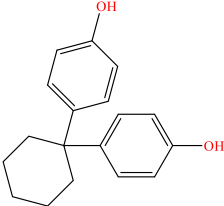
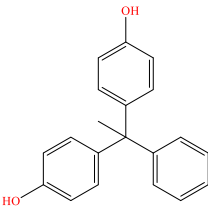
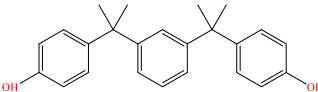
In addition, the individual CNTs and rGO particles tend to aggregate and accumulate, which limits their practical applications. To address this limitation, graphene-based porous carbon materials with 3D structure were developed [25–29]. 3D GBMs is a porous carbon material assembled by graphene-based nanomaterials under certain conditions. It not only has the characteristics of high porosity and large surface area, but also has good mechanical properties, and is easy to recover and recycle. As such, nanocomposites composed of CNTs as skeletons and graphene have demonstrated excellent potential as adsorbents/extractants in several analytical procedures. Sun and coworkers fabricated carbon aerogels with a 3D skeleton structure composed of CNTs and graphene sheets, which demonstrated excellent temperature-invariant elasticity, electrical conductivity, and absorption capacities for organic liquids [25]. Using a self-assembly method, Shen and coworkers prepared a 3D carbon material with CNTs as the skeleton, which greatly increased the mechanical strength of the graphene sheets [27]. The 3D

graphene tubes (GTs) exhibited superior adsorption capabilities for emerging and traditional pollutants (680–1729 mg/g), which were appreciably higher than those reported for previous GO and CNT-based adsorbents. The enhanced adsorption properties were attributed to the synergistic effects of GO and CNTs in structural microenvironments, nano-substrate properties, and active sites. However, individual carbon materials generally have poor hydrophilicity and few active sites. In order to further solve the problems of poor hydrophilicity and few active sites of three-dimensional carbon nanocomposites, heteroatomic doping of carbon materials has attracted the attention of researchers. The physico-chemical properties of carbon materials can be effectively modulated by heteroatomic doping, such as with N, S, and B. Among them, N atoms can preferentially enter into the lattice of carbon materials owing to their similar radius and varying electronegativity as C atoms, which makes N an ideal doping atom for carbon materials [30].

Increasing total N and N-containing functional groups in carbon materials is beneficial for improving the adsorption capacity for analytes [31]. For example, the presence of pyridine N sites plays an important role by enhancing adsorption mechanisms driven by Lewis acid-base, hydrophobic,  $\pi$ - $\pi$ , and H-bonding interactions [28]. Ding et al. fabricated magnetic N-doped graphite tubes (Ni@N-GrTs) as an extractant in an ET-MSPE procedure, and documented that pyridine N enhanced  $\pi$ - $\pi$  interaction and H-bonding with target molecules, thereby improving extraction efficiency [8]. However, the different carbon-based nanocomposites possess varying structural properties, defect sites, and N-doping types, which lead to differential adsorption/extraction efficiencies for BPs. The adsorption kinetics of carbon-based nanocomposites depend on the relationship between the specific structure of nanomaterials and the structural characteristics of the BPs [30,32,35]. While previous reports have primarily focused on the differential kinetics of BPA adsorption to CNTs, rGO, and their composites [33–35], there is a paucity of information regarding the mechanistic understanding of BP adsorption by carbon-based nanocomposites, which limits the development of new nanocomposites to improve their performance in extraction/adsorption procedures.

Fruit juices are a popular beverage throughout the world owing to their nutritional and health benefits, but these juice samples are often contaminated by BPs originating from the fruit, environmental waters, and packaging materials [9]. Due to trace levels of BPs (ng/L- $\mu$ g/L) in our dietary fruit juices, establishing accurate and rapid detection methodology is warranted to assure food safety and quality control. Building upon the previous findings, we synthesized a 3D-structure Co, Ni-codoped and a N-modified CNTs/graphene magnetic nanomaterial (CoNi-N-CNTs/rGO). This nanocomposite was inferred to possess excellent physico-chemical properties as an extractant/adsorbent owing to the strong magnetic properties of the Co, Ni alloy, more abundant absorption/defect sites due to N-doping, and a 3D multi-porous structure resulting from CNTs' in-situ growth on the graphene surface. The CoNi-N-CNTs/rGO was employed as an adsorbent/extractant for effervescence tablet-assisted magnetic solid-phase microextraction (ET-MSPE) for trace-level BP detection in fruit juices. Coupled with HPLC-FLD detection, the ET-MSPE method was successfully employed to simultaneously quantify six structural analogues of BPs (BPA, BPB, BPAP, BPZ, BPM, BPF) in six fruit juices. The underlying molecular mechanisms regulating adsorption performance were assessed based on molecular characterization (e.g., XPS, FT-IR) and DFT theoretical calculations. These findings provide a theoretical foundation for elucidating the molecular interactions between CoNi-N-CNTs/rGO and BPs. The as-constructed ET-MSPE/HPLC-FLD method integrated highly efficient adsorption, extraction and dispersion into one synchronous step, and generated excellent performance metrics for the detection of trace-level BPs in beverages.

**Table 1**  
The molecular structures, weights and selected properties of bisphenols.

Chemical name	Acronym	CAS	Chemical structure	pK <sub>a</sub>	Log K <sub>ow</sub>	Molecular weight g mol <sup>-1</sup>
2,2-bis(4-hydroxyphenyl)propane	BPA	80-05-7		10.29	3.64	228.29
4,4'-(1-methylpropylidene) bisphenol	BPB	77-40-7		10.27	4.13	242.31
bis(4-hydroxyphenyl) methane	BPF	620-92-8		9.91	2.76	200.24
4,4'-(1,1-cyclohexanediy)bisphenol	BPZ	843-55-0		9.91	4.87	268.35
1,1-bis(4-hydroxyphenyl)-1-phenylethane	BPAP	1571-75-1		9.74	4.86	290.26
1,3-Bis[2-(4-hydroxyphenyl)-2-propyl]benzene	BPM	13595-25-0		10.31	6.25	346.46

Note: Data are from reference "Bernat Oró-Nolla, Silvia Lacorte, Kristine Vike-Jonas, Susana V. Gonzalez, Torgeir Nygård, Alexandros G. Asimakopoulos and Veerle L.B. Jaspers. Occurrence of Bisphenols and Benzophenone UV Filters in White-Tailed Eagles (*Haliaeetus albicilla*) from Smla, Norway. *Toxics*, 9, 34".

## 2. Experimental section

### 2.1. Materials and reagents

Bisphenol A (BPA), bisphenol B (BPB), and bisphenol AP (BPAP), whose purities were all > 99.0%, were purchased from AccuStandard (Shanghai, China). Bisphenol Z (BPZ), bisphenol F (BPF), bisphenol M (BPM), and hexadecyltrimethyl ammonium bromide (CTAB) with purities > 99.0% were obtained from Sigma-Aldrich (Shanghai, China). Table 1 lists selected physico-chemical properties of the BPs including chemical name, CAS No., molecular structure, pK<sub>a</sub>, molecular weight, and log<sup>K<sub>ow</sub></sup>. Analytical-grade (AR) melamine, cobalt chloride hexahydrate (CoCl<sub>2</sub>·6H<sub>2</sub>O), and nickel acetate tetrahydrate (Ni(CH<sub>3</sub>COO)<sub>2</sub>·4H<sub>2</sub>O) were purchased from Adamas Reagent (Beijing, China) and used as received. Graphene oxide (GO) was acquired from Nanjing Xianfeng Nano Materials (Nanjing, China). Chromatographic-grade (GR) acetonitrile, methanol, and acetone were procured from Tedia (Shanghai, China). L-(+)-tartaric acid (TTA) and anhydrous sodium carbonate (Na<sub>2</sub>CO<sub>3</sub>) were of analytical-grade (AR) and purchased from Sinopharm (Shanghai, China). Stock solution of each BP (1.0 mg/mL) was prepared in methanol and stored at 4 °C. Dilution of stock solutions with ultrapure water was used to prepare same-day working solutions. A Milli-Q Ultrapure water system (Bedford, MA, USA) was used to generate ultrapure water (>18.2 MΩ).

### 2.2. Real-world juice samples

Six commercial juice samples, including peach, pear, plum, pomelo tea, orange, and lactobacillus, were gratis supplied by a local Haoyouduo supermarket (Suzhou, China). An aliquot (5 mL) of each juice sample was diluted to 10 mL with ultrapure water and transferred to a 50-mL centrifuge tube. The diluted sample was vortexed for 2 min, and then centrifuged at 5,000 r/min for 5 min. Finally, the resultant solution was filtered through a 0.45-μm membrane, and the supernatant immediately used for the ET-MSPE procedure, or stored at 4 °C for use within one week.

### 2.3. Analytical instrumentation and methods

Morphology of the CoNi-N-CNTs/rGO was imaged with transmission electron microscopy (TEM, G2 F30, Tecnai, OR, USA) and scanning electron microscopy (SEM, quanta250, FEI, USA). The crystalline structure of the nanomaterials was determined using an X-ray diffractometer (XRD) (Bruker D8 Advance, Billerica MA, USA). A Nicolet 6700 FTIR spectrometer (Thermo Fisher, NY, USA) was used to record the FT-IR spectra of nanomaterials and Raman spectra were acquired by a DXR SmartRaman spectrometer (Thermo Fisher, NY, USA). X-ray photoelectron spectroscopy (XPS) was conducted on a Thermo Fisher scientific probe spectrometer. Magnetic properties were measured with a

Quantum Design MPMS XL-7 Superconducting Quantum Interference Device (SQUID) (Olomouc, Czech Republic). Specific surface area (BET) and pore size distribution (BJH) were acquired on a Micromeritics adsorption analyser (Tristar 3030, NY, USA).

HPLC-FLD detection was conducted using a Shimadzu LC system equipped with a SIL-20A autosampler, LC-20AT pump, and RF-20A fluorescence detector (Shimadzu, Kyoto, Japan). To separate the analytes, Shim-pack GIST C<sub>18</sub> columns (5  $\mu$ m, 4.6  $\times$  250 mm; Shimadzu, Japan) were utilized with acetonitrile (A) and water (B) comprising the mobile phase using a gradient program (0–9 min, 50% A and 50% B, 9–20 min, 70% A and 30% B) with detector excitation and emission wavelengths of 233 and 303 nm, respectively. The HPLC procedure was run with a flow rate of 1.0 mL min<sup>-1</sup> at 30 °C and injection volume of 10  $\mu$ L.

#### 2.4. Synthesis of CoNi-N-CNTs/rGO nanocomposites

CoNi-N-CNTs/rGO nanocomposites were fabricated using a facile calcination method. First, 0.5 g of CTAB and 5 g of tripolycyanamide were dissolved in 40 mL of ultrapure water and stirred magnetically for 30 min at 600 r/min at 80 °C to homogeneously mix the two precursors (termed A solution). Second, 10 mL of solution, containing 0.4 g of CoCl<sub>2</sub>·6H<sub>2</sub>O and 0.4 g of Ni(CH<sub>3</sub>COO)<sub>2</sub>·4H<sub>2</sub>O, were dropwise added to the A solution with continuous stirring (termed B solution). Third, an aqueous solution of GO was prepared by adding 10 mg of GO to 30 mL of ultrapure water followed by a 30-min ultrasonication. The resulting GO solution was dropwise added to the mixed B solution under continuous ultrasonic mixing. A lavender-colored precursor was obtained by freeze-drying after stirring at 500 r/min for 10 h. After grinding, the precursor material was transferred to a porcelain boat and placed in a tube furnace under gentle flow of ultrapure N<sub>2</sub>. After heating the sample to 500 °C for one hour using a 2.5 °C/min heating rate, the material was then heated to 900 °C using a 5 °C/min heating rate, and finally held at 900 °C for one hour. After natural cooling to ambient temperature, the resulting black powder was collected and washed several times with ultrapure water and alcohol, and then oven-dried at 60 °C for 8 h. The Ni-N-CNTs/rGO and Co-N-CNTs/rGO nanocomposites were prepared using the same protocols as CoNi-N-CNTs/rGO, but in the absence of cobalt and nickel, respectively.

#### 2.5. Preparation of effervescent tablets and the ET-MSPE procedures

Fabrication of effervescent tablets utilized three precursors, including CoNi-N-CNTs/rGO (7.4 mg) as adsorbent and extractant, TTA (150 mg) as the acidic source, and Na<sub>2</sub>CO<sub>3</sub> (106 mg) as the alkaline source. The precursors were uniformly mixed in a mortar and the powder compressed into tablets with a hand-operated T5 Single Punch Press (Kunshan, China). Once prepared, effervescent tablets (8-mm diameter  $\times$  2.5-mm thickness) were sealed in a moisture-proof cabinet.

A 5-mL aliquot of the pretreated sample solution was placed in a 15-mL plastic centrifuge tube. An effervescent tablet was dropped into the centrifuge tube resulting in vigorous CO<sub>2</sub> bubbles that effectively dispersed the CoNi-N-CNTs/rGO nanomaterial. The effervescent reaction persisted for ~ 3–5 min at ambient conditions. Subsequently, the CoNi-N-CNTs/rGO extractant/adsorbent was collected by placing an external magnet along the test tube wall. The supernatant was discarded, and the remaining nanoparticles were eluted/re-dissolved in an appropriate volume of acetone. Lastly, the eluent was evaporated under a gentle N<sub>2</sub> flow and re-dissolved in 400  $\mu$ L of acetonitrile before filtration through a 0.22- $\mu$ m membrane filter and analytical quantification with HPLC-FLD (Fig. 2a).

#### 2.6. Screening important operational parameters by Plackett-Burman design (PBD)

PBD is a preferred design approach for screening and evaluating the

important operational variables influencing the experimental response. By varying all the influencing factors in a limited number of experiments, this statistical method is conducive to quantifying the relationship among influencing factors [36]. PBD is commonly used to determine which variables significantly affect the extraction recoveries (ERs) for analytes. In this study, we assessed five operational variables (temperature (A), elution time (B), amount of extractant (D), pH (E), and elution volume (F)) and one dummy variable (C) using a 12-run PBD (Table S1). Two levels of each variable were considered (-1 for the low level and +1 for the high level) based on preliminary experiments.

#### 2.7. Multi-factor interaction analysis by central composite design (CCD)

We used a second-order multivariate technique utilizing CCD with a multi-level factorial design incorporating axial points and central points for all factors along with a center coding to determine a response surface for optimization of the analytical performance [8,36]. Based on the aforementioned PBD results, a CCD experiment, including 16 treatments at five levels ( $-\alpha$ ,  $-1$ ,  $0$ ,  $+1$ ,  $+\alpha$ ) for each factor, was used to investigate multi-factor interactions. All optimization experiments were evaluated based on the average ERs for the six BPs (Table S2). The significance of main variables and their interactions was determined using Design-Expert 8.0.5 software (Minneapolis, USA) and analysis of variance (ANOVA).

#### 2.8. Analytical performance of the ET-MSPE/HPLC-FLD method for real-world juice samples

The performance of the newly developed method was evaluated based on a series of analytical metrics, including linear range (LR), determination coefficient (R<sup>2</sup>), precision, accuracy, limit of detection (LOD, based on S/N = 3), limit of quantification (LOQ, based on S/N = 10), and ER. These analytical metrics were acquired using the optimized operational conditions determined by CCD. To investigate potential matrix effects, the six juices (peach, pear, plum, pomelo tea, orange, and lactobacillus beverage) were spiked with BPs at three fortification levels (5, 20, and 200  $\mu$ g/L), and each spiking experiment was conducted with three replicates. Further, six parallel experiments were conducted to determine intra-day and inter-day relative standard deviations (RSDs).

#### 2.9. Adsorption experiments

Briefly, 100 mL of the six mixed BP solutions (C<sub>0</sub> = 5 mg/L) were added to a 250 mL conical flask to which 5 mg of CoNi-N-CNTs/rGO was added. The flask was shaken at 200 r/min in a constant-temperature shaker at 25 °C. At 3, 5, 10, 30, 60, 90, and 120 min, an aliquot (1 mL) of the mixed solution was collected, and the adsorbent was separated from the sample solution with a magnet. Finally, the BP concentrations remaining in solution were quantified by HPLC-FLD, using three replicates for each treatment.

#### 2.10. Density functional theory (DFT) calculation

Structural optimization and ground-state energies were calculated using the Gaussian 16 program. We selected B3LYP for functional analysis, 6–31 g(d) for non-metallic element basis, “Tight” for the self-consistent field (SCF) and structural optimization convergence criteria, and 6–311 g(d,p) for the energy calculation. To describe weakly bound molecular systems, the density functional dispersion correction (DFT-D3) method of Grimme was adopted with Becke-Johnson damping.

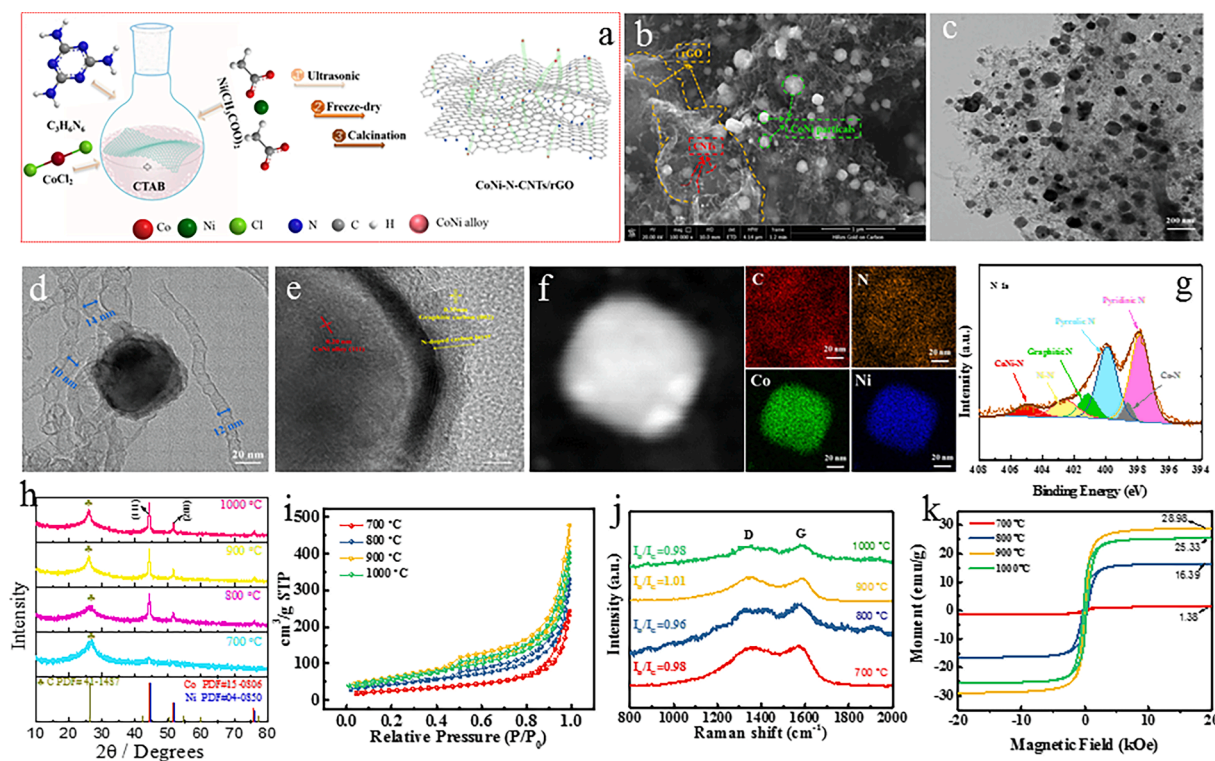


**Fig. 1.** Morphology and structural characterization. (a) Schematic for formation of CoNi-N-CNTs/rGO; (b) SEM image for CoNi-N-CNTs/rGO; (c), (d), (e) TEM images for CoNi-N-CNTs/rGO; (f) elemental (EDS) mapping of C, N, Co and Ni; (g) N1s XPS spectrum for CoNi-N-CNTs/rGO; (h) XRD patterns at various temperatures; (i)  $N_2$  adsorption/desorption isotherms at various temperatures; (j) Raman spectrum at various temperatures; and (k) Magnetic hysteresis loops at various temperatures.

### 3. Results and discussion

#### 3.1. Morphological and structural characterization of as-prepared nanomaterials

##### 3.1.1. Structural analyses of intermediate nanocomposite materials

To fabricate the 3D CoNi-N-CNTs/rGO nanocomposites, we carbonized the freeze-dried mixture of reaction precursors at high temperature under a  $N_2$  atmosphere (Fig. 1a). The functional groups and elemental composition of the CoNi-N-CNTs/rGO-500 formed at a calcination temperature of 500 °C were verified by FT-IR and XPS analyses. Major FT-IR absorption peaks appeared at 804, 1250–1670, and 3070–3280  $cm^{-1}$  (Fig. S1a). These absorption peaks were assigned to bending vibrations of the triazine ring structure at 804  $cm^{-1}$ , C-N heterocyclic compound stretching between 1250 and 1670  $cm^{-1}$ , and N-H species in the g- $C_3N_4$  at 3070–3280  $cm^{-1}$  [37].

The full XPS spectrum and deconvolution spectra of C1s, N1s, Co2p and Ni2p for the intermediate CoNi-N-CNTs/rGO-500 material are shown in Fig. S1b–f. Distinct peaks at 285.8, 400.6, 531.4, 780.08 and 855.05 eV in the full XPS spectra were assigned to C1s, N1s, O1s, Co2p and Ni2p, respectively (Fig. S1b). In the deconvolution C1s spectrum, the peaks at  $\sim 284.4$ ,  $\sim 285.7$ , and  $\sim 288.5$  eV were attributed to C–C, C–N, and C–O bonds, respectively (Fig. S1c). The three peaks in the N 1s signal at 398.4, 399.2 and 400.6 eV (Fig. S1d) were ascribed to sp<sup>2</sup>-hybridized nitrogen (C = N–C), tertiary nitrogen (N–(C)<sub>3</sub>), and amino functional groups (C–N–H), respectively. These structural characteristics for the intermediate product obtained at 500 °C document the formation of g- $C_3N_4$  from the transformation of melamine. Further, XPS analysis of cobalt and nickel (Fig. S1e and Fig. S1f) indicated peaks for Co<sup>0</sup> (780.2 eV and 795.9 eV) and Ni<sup>0</sup> (854.4 eV and 871.8 eV) in the intermediate compounds. Overall, the cobalt and nickel salts were gradually transformed into seeds of the cobalt–nickel alloy [37,38], which provide the foundation for generating a cobalt–nickel alloy with excellent magnetic

properties upon further heating to 900 °C.

##### 3.1.2. Morphological and structural analyses of CoNi-N-CNTs/rGO nanocomposite

The morphology and structure of the nanocomposites after heating to 900 °C were observed by SEM and TEM (Fig. 1b–e and Fig. S2a). C-nanotubes appeared to grow on the surface of the rGO with lengths of  $\sim 1$ –10  $\mu m$ . The overall morphology showed a three-dimensional (3D) structure with nanotubes sandwiched between the sheets. The nanoparticles had an average diameter of  $\sim 65$  nm and were wrapped/encapsulated in the carbon material. The HRTEM observation showed a 0.20-nm lattice spacing with the (111) crystal face of CoNi alloy, and the outer fringe spacing (0.35 nm) corresponds to the (002) plane of graphite. Energy dispersive spectroscopy (EDS) mapping of the elemental distribution was performed on the CoNi-N-CNTs/rGO (Fig. 1f). The Co and Ni were evenly distributed in the nanoparticles, and the N was distributed throughout the carbon layer. XPS analysis was further used to characterize the N forms in the carbon layers. Based on the high-resolution N1s image (Fig. 1g), six types of N were deconvoluted at 398.0, 398.8, 400.2, 401.2, 402.6, and 404.5 eV, corresponding to pyridinic N, Co-N, pyrrolic N, graphitic N, Ni-N, and CoNi-N, respectively. N doping can introduce structural defects in carbon materials that provide an abundance of  $\pi$  electrons to enhance  $\pi$ - $\pi$  conjugation, thereby enhancing adsorption properties, increasing adsorption sites for CoNi-N-CNTs/rGO, and improving the adsorption performance for BPs [29,32].

##### 3.1.3. Effect of heating temperature on nanomaterial properties

Heating temperature has a strong influence on the formation of magnetic particles and N doping in nanomaterials [34,37]. Generally, high temperature is conducive to the doping of heteroatoms, and thus the structure and physicochemical properties of the CoNi-N-CNTs/rGO. Hence, we determined the effects of different calcination temperatures

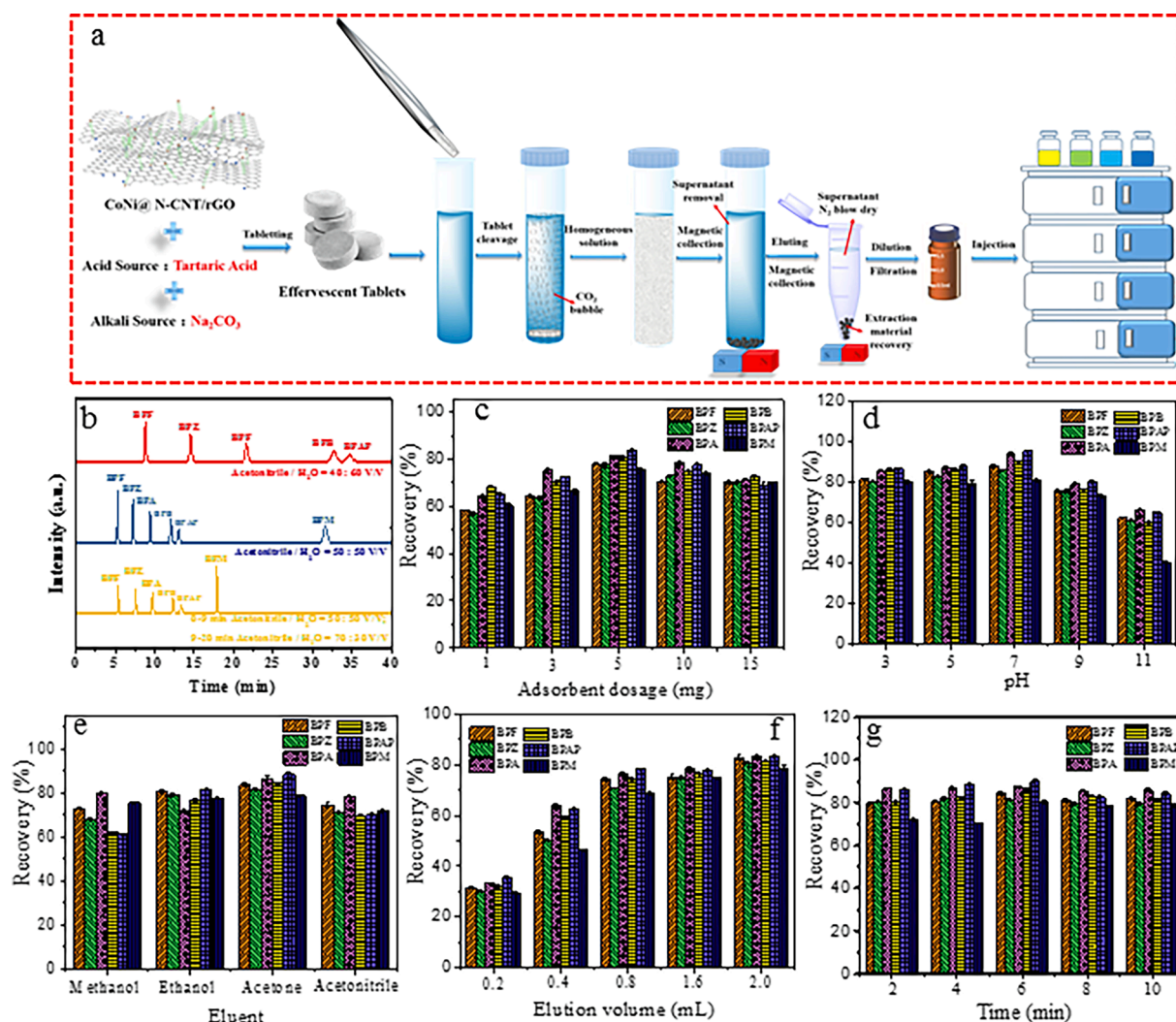


**Fig. 2.** The overall operational procedures of the ENCG/HPLC-FLD method (a) and effects of the main operational variables on ERs for BPs: (b) composition of the mobile phase; (c) dosage of adsorbent; (d) pH; (e) type of elution solvent; (f) volume of elution solvent; and (g) elution time. **Notes:** Error bars represent the standard deviation ( $n = 3$ ).

(700, 800, 900, and 1,000 °C) on the resulting CoNi-N-CNTs/rGO product. XRD patterns displayed broad peaks at  $2\theta = 26.4^\circ$  for all calcination temperatures (Fig. 1h), which were ascribed to the (002) plane of graphite (PDF#41-1487). The Co and Ni peaks are not obvious at 700 °C, but with further increases in calcination temperature from 800 to 1,000 °C, the peaks at  $44.4^\circ$ ,  $51.7^\circ$  and  $76.1^\circ$  were gradually enhanced. Two distinct peaks, corresponding to cubic Co (PDF#15-0806) and cubic Ni (PDF#04-0850), were indexed to the (111) and (200) planes of CoNi alloy, respectively (Fig. 1h). These findings provide compelling evidence that the nanoparticles in the 3D CoNi-N-CNTs/rGO nanocomposites have a Co-Ni alloy structure/composition.

Nitrogen adsorption-desorption isotherms were determined across the calcination temperature range to examine surface area and pore-size distribution. As shown in Fig. 1i, the Brunauer-Emmett-Teller (BET) surface area of 3D CoNi-N-CNTs/rGO was  $226.63 \text{ m}^2/\text{g}$  at 900 °C, which was substantially larger than those at 700 °C ( $95.26 \text{ m}^2/\text{g}$ ), 800 °C ( $155.11 \text{ m}^2/\text{g}$ ), and 1,000 °C ( $213.10 \text{ m}^2/\text{g}$ ). The pore diameter was mainly distributed in the mesoporous range of 2.2–2.4 nm (Fig. S2b). As compared to Co-N-CNTs/rGO ( $255.22 \text{ m}^2/\text{g}$ ) and Ni-N-CNTs/rGO ( $320.95 \text{ m}^2/\text{g}$ ) (Fig. S2c-d), the specific surface area of the bimetallic co-doping nanomaterial was smaller. This phenomenon may result from the Co-Ni alloy nanoparticles occupying more voids in the nanomaterial,

thereby leading to a decrease in specific surface area.

Raman spectra of nanocomposites were examined across the calcination temperature range and metal doping treatments (Fig. 1j and Fig. S2e). The  $I_D/I_G$  values at 700, 800, 900, and 1,000 °C were 0.95, 0.96, 1.01, and 0.98, respectively, while those of Co-N-CNTs/rGO and Ni-N-CNTs/rGO at 900 °C were 0.95 and 1.02. The  $I_D/I_G$  value of CoNi-N-CNTs/rGO at 900 °C was similar to that of Ni-N-CNTs/rGO, but higher than those at other temperatures (700, 800, and 1,000 °C). We interpret these data as evidence that the bimetal and N co-doping nanocomposites have a higher degree of disorder and more defect sites, which is beneficial to the rapid and efficient adsorption of BPs.

The vibrating sample magnetometer (VSM) characterization of the as-prepared nanocomposites at varying temperatures and metal doping treatments are displayed in Fig. 1k and Fig. S2f. The maximum saturation magnetization ranged from 1.38 to 28.98 emu/g as the calcination temperature increased from 700 to 1,000 °C. Among the calcination temperatures, the highest magnetism (28.98 emu/g) of CoNi-N-CNTs/rGO occurred at 900 °C, which was  $\sim 1.3$ – $2.0$  fold higher than those of Co-N-CNTs/rGO (12.42 emu/g) and Ni-N-CNTs/rGO (9.63 emu/g). In the ET-MSPE procedure, the excellent magnetic properties of CoNi-N-CNTs/rGO fully satisfied the technical requirement for effective and convenient separation using an external magnet. Based on the overall nanocomposite properties and feasibility for practical application, the

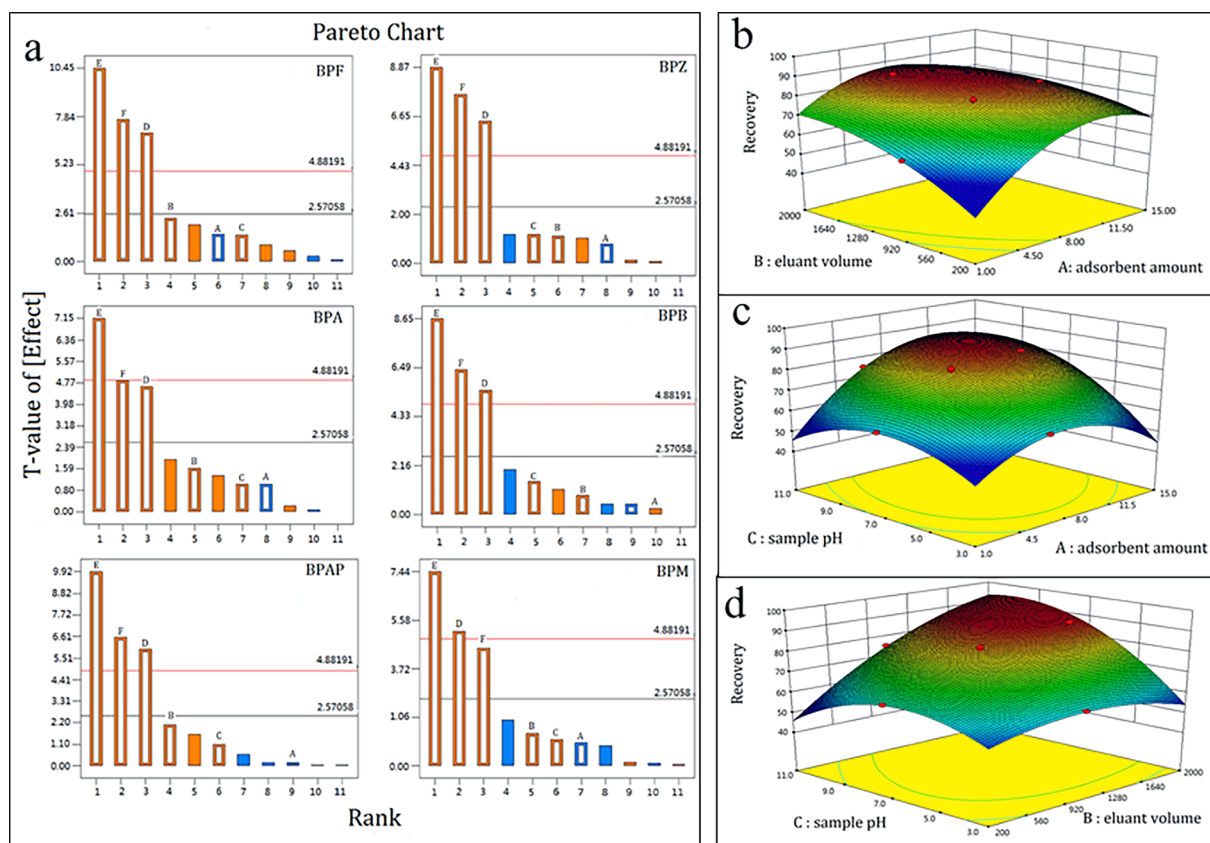


**Fig. 3.** (a) Pareto charts for the effects of the six operational variables on ERs for BPs; (b) 3D-response surface for extraction solvent volume and dosage of adsorbent at pH = 7.0 on average ERs; (c) 3D-response surface for pH and dosage of adsorbent at 2000  $\mu\text{L}$  extraction solvent on average ERs; and (d) 3D-response surface for pH and extraction solvent volume at 5 mg dosage of adsorbent on average ERs. **Notes:** Variables with  $t$ -values higher than the critical value (2.57) are regarded as statistically significant factors.

calcination temperature of 900 °C was selected for the synthesis of the nanocomposites.

### 3.2. Optimization of the ET-MSPE/HPLC-FLD procedures

#### 3.2.1. Single factor optimization using the one-factor-at-a-time approach

The effervescent tablet was composed of three components, the synthesized nanocomposites as adsorbent/extractant, acidic source, and alkaline source. The pressed tablets were utilized in the ET-MSPE procedures to examine several factors influencing the adsorption/extraction efficiencies for BPs, such as dosage of extraction/adsorbent, solution pH, eluent type, elution time, and extraction time. In addition, the composition and ratio of the mobile phase in the HPLC-FLD influenced the chromatographic separation of the six BPs. As illustrated in Fig. 2b, the six BPs (BPF, BPZ, BPA, BPB, BPAP, and BPM) were effectively separated with high resolution and presented sharp and symmetrical peaks under gradient elution with acetonitrile and water: 50%/50% by v/v at 0–9 min and 70%/30% by v/v at 9–20 min. Compared to isocratic elution (acetonitrile–water 50%/50% or 40%/60% by v/v), retention times for the six BPs were prominently shortened to < 20 min under the gradient-elution conditions.

We examined whether the nanomaterial-based adsorbent/extractant dispersed better with or without CoNi-N-CNTs/rGO-based effervescent reaction by comparing the ERs for the six BPs (Fig. S3). Effervescent tablets prominently improved ERs (ca. 85%), which was significantly higher than in the absence of effervescent tablets (ca. 72%). The presence of vigorous  $\text{CO}_2$  bubbles produced by the effervescent reaction was effective in dispersing the nanocomposites, thereby enhancing the ERs for all BP analytes. Moreover, the CoNi-N-CNTs/rGO-based effervescent tablet is portable and eliminates the need for an external physical energy

source, such as shaking, ultrasound, or vortexing, making the procedure more suitable for remote/outdoor use.

Too little or too much extractant/adsorbent will lead to insufficient adsorption or low extractability in the subsequent elution process, thereby substantially reducing ERs [22]. Hence, the dosage of the CoNi-N-CNTs/rGO nanocomposite has a significant effect on the ERs for BPs (Fig. 2c). When the dosage increased from 1 to 5 mg, the average ERs rose gradually from 62.3 to 79.4%; however, further increases in dosage from 5 to 15 mg resulted in a slight decrease of average ERs. This phenomenon can be explained by the reduced dispersion efficiency or to lower extractability of analytes in the subsequent elution process owing to excessive extractant/adsorbent [8,22]. Based on this optimization trial, 5 mg of CoNi-N-CNTs/rGO nanocomposite was used in subsequent analyses.

Initial solution pH is an important operational variable in the ET-MSPE procedure since it determines the surface charge of the extractant/adsorbent, ionization degree, and adsorbent specificity. Based on previous reports [8,36], the extraction efficiency was investigated over a pH range of 3.0–11.0 (Fig. 2d). The highest average ERs were observed at pH 7.0; under such circumstances, the ERs for BPZ, BPA, and BPM were all > 90%. Notable, the ERs significantly declined under strongly alkaline conditions (pH 9.0 or 11.0). For example, the average ERs for BPs decreased to as low as 58.3% when the initial solution pH was 11.0, owing to the ionization of BPs under alkaline conditions.

After effervescent-assisted extraction, the nanocomposites with adsorbed BPs were collected at the bottom of test tube using an external magnet. Subsequently, the supernatant was discarded, and the collected nanomaterial was eluted with an appropriate eluent to release the BPs for quantification (Fig. 2a). Four eluents (methanol, ethanol, acetone, and acetonitrile) were assessed for their elution efficiencies. The average



**Table 2**  
Analysis of variance (ANOVA) for quadratic response surface model.

	SS	df	MS	F-value	p-value	Significance
Block	6.8	1	6.8		Probe > F	
Model	1988.4	9	220.9	177.0	< 0.0001	Significant
D	133.2	1	133.2	106.7	0.0001	
E	15.1	1	15.1	12.5	0.0010	
F	57.7	1	57.7	46.2	0.0166	
DE	31.9	1	31.9	25.5	0.0039	
DF	188.4	1	188.4	150.9	< 0.0001	
EF	78.2	1	78.2	62.7	0.0005	
D <sup>2</sup>	324.9	1	324.9	260.2	< 0.0001	
E <sup>2</sup>	700.4	1	700.4	561.0	0.0001	
F <sup>2</sup>	143.4	1	143.4	114.8	< 0.0001	
Residual	6.2	5	1.3			
Lack-of-Fit	2.997E-003	1	2.997E-003	1.921E-003	0.9671	
Pure Error	6.2	4	1.6			
Cor Total	200.5	15				

$$Y = -144.92 - 249.39D + 25.67E - 34.03F - 31.54DE - 19.20DF - 5.42EF - 86.84D^2 - 10.11E^2 - 2.04F^2.$$

ERs provided by the elution solvents followed: acetone > ethanol > acetonitrile > methanol (Fig. 2e). Since the Log<sup>K<sub>ow</sub></sup> of acetone (5.4) is close to that of moderately polar BPs (Log<sup>K<sub>ow</sub></sup> = 2.76–6.25, Table 1), acetone offered the highest elution efficiencies for the BPs.

When the volume of acetone increased from 0.2 to 0.8 mL, the average ERs rose rapidly from ~31.2 to 73.6%, implying an insufficient volume for elution of BPs at the lower volumes (Fig. 2f). With further increases in acetone volume (0.8–2.0 mL), the average ERs rose gradually, and reached a plateau (~81.7%) at 2.0 mL (Fig. 2f). Based on these findings, we selected 2 mL of acetone as an optimum elution solvent volume. As the elution time increased from 2 to 6 min, the average ERs increased gradually from 80.8 to 84.7% (Fig. 2g). However, at elution times > 6 min, there was a slight decrease in average ERs from 84.7 to 81.6% (Fig. 2g). These observations demonstrate that adsorption–desorption equilibrium was attained at ~6 min, which we adopted as our optimum elution time.

### 3.2.2. Screening the key operational factors by Plackett-Burman design (PBD)

The Pareto charts based on PBD showed that temperature, elution time, and the dummy factor did not have significant effects on average ERs (Fig. 3a). In contrast, adsorbent amount (D), solution pH (E), and eluent volume (F) had significant effects ( $p < 0.05$ ) on the extraction/adsorption process. The critical value ( $t$ -value limit) for the six BPs was 2.57, which represents the significant influence of each factor at the 95% confidence level. If the variable value exceeded the  $t$ -value limit, it had a significant influence on extraction efficiency. Notably, the response of the dummy factor (C) was not significant, which indicates that the influence of unknown variables or system errors in the design process were not significant. Hence, we conclude that adsorbent amount, solution pH, and eluent volume were the most important variables for subsequent CCD optimization.

**Table 3**  
Analytical performance of the proposed method for bisphenol quantification.

Analyte	LRs (μg/L)	Calibration equation	R <sup>2</sup>	LODs (μg/L)	LOQs (μg/L)	Intra-day RSD (%; n = 6)			Inter-day RSD (%; n = 6)		
						Low	Medium	High	Low	Medium	High
BPF	0.66–500	y = 3341.5x - 264.37	0.9993	0.11	0.36	3.4	1.4	1.5	4.8	4.4	3.9
BPZ	0.60–500	y = 3039.8x + 49492	0.9977	0.18	0.60	1.8	4.3	4.0	3.5	2.9	2.3
BPA	0.66–500	y = 3319.9x + 29072	0.9966	0.20	0.66	2.6	4.8	2.8	3.5	2.8	2.0
BPB	0.63–500	y = 2835.3x + 59343	0.9966	0.18	0.60	3.8	2.1	3.2	5.4	5.0	3.2
BPAP	1.00–500	y = 1687.3x + 70504	0.9936	0.10	0.33	2.6	1.4	4.0	2.7	2.1	2.5
BPM	0.33–500	y = 7587.8x + 556893	0.9950	0.06	0.20	2.4	3.4	2.0	1.7	3.9	2.9

Note: LR, Linear ranges; R<sup>2</sup>, coefficients of determination for linear regression; LODs, limits of detection at S/N = 3; LOQs, Limits of quantitation at S/N = 10; RSD, relative standard deviation (n = 6). The detailed experimental conditions are as follows: (1) BP standards were fortified in peach juice as a representative juice example; (2) extraction process: 150 mg of TTA and 106 mg Na<sub>2</sub>CO<sub>3</sub> as precursors of an effervescent tablet, 7.4 mg of CoNi-N-CNTs/rGO as extractant, pH = 6.8, 1638 μL of acetone as eluent solution and 6 min extraction time.

### 3.2.3. Optimization by central composite design

We used CCD to simultaneously optimize the significant factors identified by PBD and analyze their interactions [8,36]. The resulting CCD model was significant ( $p = 0.9671$ ), whereas the lack of fit was not significant, suggesting that other variables had little influence on the average ERs (Table 2). The degree of fit for the polynomial model was strong (R<sup>2</sup> = 0.9969 and adjusted R<sup>2</sup> = 0.9912) demonstrating an excellent CCD model fit. All three operational variables all had a significant effect ( $p < 0.05$ ) on average ER values, consistent with the results obtained by PBD.

The resulting polynomial model describing the significant operational variables and their interactions on average ERs was:

$$Y = -144.92 - 249.39D + 25.67E - 34.03F - 31.54DE - 19.20DF - 5.42EF - 86.84D^2 - 10.11E^2 - 2.04F^2 (1).$$

where Y is the average ERs for the six BPs, the + or - before each coefficient represents a positive or negative relationship between the factor and average ERs, and the absolute value of the coefficient indicates the magnitude of factor response (Fig. S4a). Both predicted and actual data points were located near the regression line, suggesting that the model fit between actual and predicted values was strong (Fig. S4b).

The 3D response surface for the CCD show the relationship among the three operational variables and the average ERs (Fig. 3b-d). The average ERs for the six BPs changed with varying adsorbent dosage and eluent volume when the solution pH was 7.0. As the dosage rose from 1 to 7.4 mg, and eluent volume increased from 200 to 1638 μL, the average ERs increased gradually. However, when the eluant volume increased from 1,638 to 2,000 μL, the average ERs declined (Fig. 3b). At a constant eluant volume of 2,000 μL, the maximum average ERs were acquired when the adsorbent dosage increased from 1 to 9.6 mg and solution pH rose from 3.0 to 6.8 (Fig. 3c). As demonstrated in Fig. 3d, the average ERs reached a plateau at an adsorbent dosage of 5 mg, eluant volume of 1638 μL, and pH of 6.8. Consequently, the optimized values

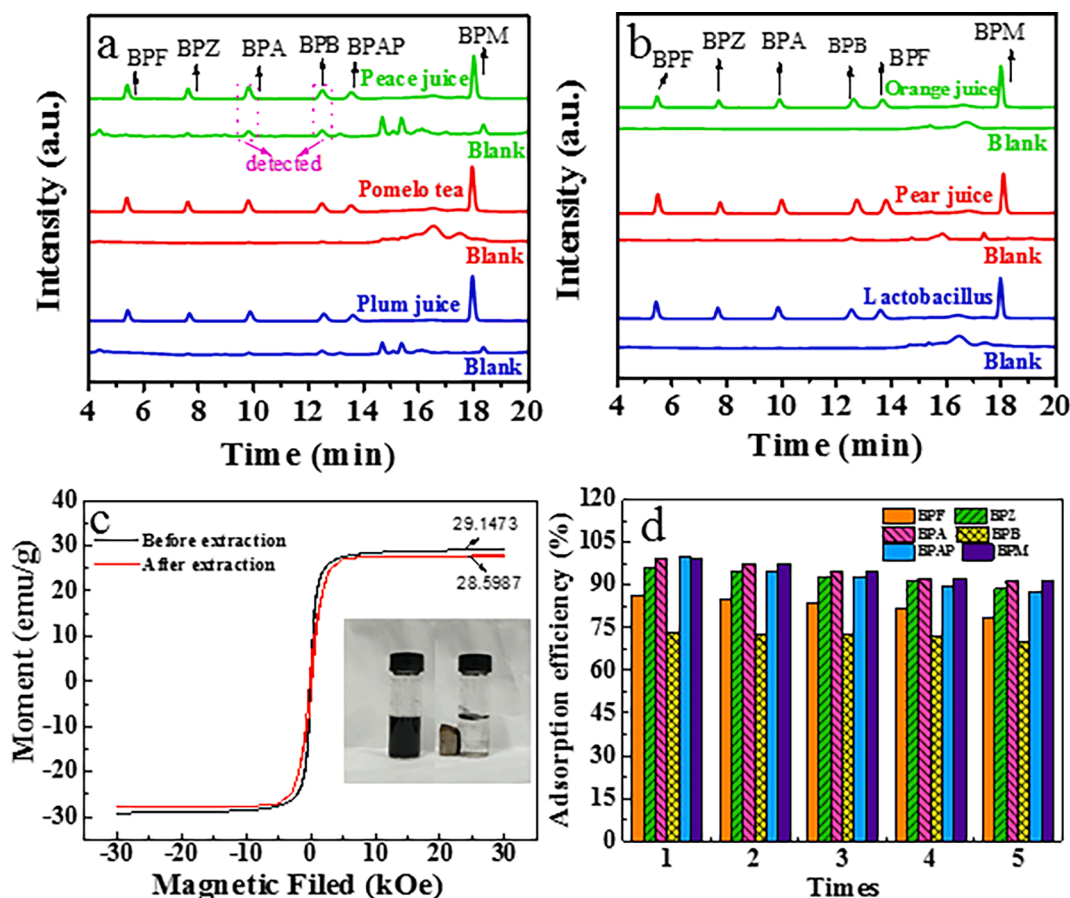


**Fig. 4.** HPLC chromatograms for blank and BP-spiked juice samples (a, b); (c) magnetic characteristics of CoNi-N-CNTs/rGO before and after adsorption of BPs; and (d) effects of repeated usage of CoNi-N-CNTs/rGO on BP adsorption. **Notes:** (1) The fortified level of BPs was  $20.0 \mu\text{g L}^{-1}$ ; and (2) experimental conditions were 150 mg of TTA and 106 mg  $\text{Na}_2\text{CO}_3$  as components of effervescent tablet, 7.4 mg of CoNi-N-CNTs/rGO as extractant,  $\text{pH} = 6.8$ , 1638  $\mu\text{L}$  of acetone as eluent solution and 6 min extraction time.

for the ET-MSPE procedures were adopted as: solution  $\text{pH}$ , 6.8; eluent volume, 1638  $\mu\text{L}$ ; and adsorbent dosage amount, 7.4 mg.

### 3.2.4. ET-MSPE/HPLC method evaluation

To evaluate the analytical performance of the ET-MSPE/HPLC method under optimized conditions (7.4 mg of CoNi-N-CNTs/rGO as extractant, solution  $\text{pH} = 6.8$ , 1638  $\mu\text{L}$  of acetone as eluent solvent, and 6-min extraction time), the following metrics were determined: linear range (LR), coefficient of determination ( $R^2$ ), limits of detection (LODs, based on  $S/N$  of 3), limits of quantification (LOQs, based on  $S/N$  of 10), and intra-day/inter-day precision (Table 3). Standard curves for the six BPs displayed a good LR (0.33–500  $\mu\text{g/L}$ ) with  $R^2$  values of 0.9936–0.9993. The LODs and LOQs were 0.06–0.20  $\mu\text{g/L}$ , and 0.20–0.66  $\mu\text{g/L}$  for the six BPs, respectively. Method precision was evaluated from intra-day and inter-day relative standard deviations (RSDs) at three levels of BP fortification (5, 20, and 200  $\mu\text{g/L}$ ). The RSDs ranged between 1.4 and 4.8% for intra-day precision and from 1.7 to 5.4% for inter-day precision indicating a high level of experimental precision (Table 3).

### 3.2.5. Analysis of the real-world juice samples by the ET-MSPE/HPLC-FLD method

To demonstrate the feasibility of the newly developed method for real-world juice samples, we determined trace-level BPs in six boxed beverages. Typical chromatograms for the six juice samples at a fortification level of 20  $\mu\text{g/L}$  are exhibited in Fig. 4a–b. The six BPs (BPF, BPZ, BPA, BPB, BPAP, BPM) were well separated with high resolution within a 20 min runtime. The ERs spanned the range of 82.4–103.7% across the

three fortifications levels (5.0, 50.0 and 200.0  $\mu\text{g/L}$ ). BPA and BPB were only detected in peach juice at 2.09 and 1.37  $\mu\text{g/L}$ , respectively, whereas no other BPs were detected in the non-fortified juice samples (Table 4). These data/findings demonstrate that the ET-MSPE/HPLC-FLD method is a highly accurate and precise technique for efficient detection of common BPs at trace levels in real-world juice samples.

### 3.2.6. Magnetic and sorption changes with regenerative use

Magnetic hysteresis loops for the CoNi-N-CNTs/rGO nanocomposite were measured before/after extraction/adsorption across the temperature range from 2 to 400 K. Saturation magnetization of CoNi-N-CNTs/rGO before and after an adsorption cycle was 29.15 and 28.59 emu/g, respectively (Fig. 4c). The nanocomposites were uniformly dispersed and conveniently separated by an external magnetic field (picture inserted in Fig. 4c). The nanomaterial was separated by a magnet, alternately washed three times with ethanol and ultrapure water, and dried at 60 °C. The recycled nanocomposite was then used in another extraction/adsorption cycle. After five extraction/adsorption cycles, the loss of adsorption efficiency for the six BPs varied between 3.1 and 12.4% (Fig. 4d), which proved that this nanocomposite (CoNi-N-CNTs/rGO) possessed excellent recyclability and stability.

### 3.2.7. Mechanisms for extraction/adsorption of BPs by CoNi-N-CNTs/rGO

Multistage mesoporous structures existed in 3D CoNi-N-CNTs/rGO nanomaterials and abundant pore structures promoted the adsorption of target molecules. Adsorption isotherms and kinetics for BP sorption by CoNi-N-CNTs/rGO nanocomposite were analyzed in detail. The adsorption capacity ( $Q_e$ ) for the six BPs by CoNi-N-CNTs/rGO increased

**Table 4**  
Analytical performance of the proposed method in real juice samples.

Samples	BPF			BPZ			BPA			BPB			BPAP			BPM					
	Blank	Added µg/L	ERS %	RSDs %	Blank	Added µg/L	ERS %	RSDs %	Blank	Added µg/L	ERS %	RSDs %	Blank	Added µg/L	ERS %	RSDs %	Blank	Added µg/L	ERS %	RSDs %	
Peach juice	ND	5.0	94.6 ± 2.1	2.2	ND	5.0	93.4 ± 3.8	4.1	2.09	5.0	86.2 ± 4.3	5.0	1.37	5.0	92.3 ± 2.7	2.9	ND	5.0	90.0 ± 1.9	2.1	ND
		20.0	87.2 ± 4.3	4.9		20.0	94.7 ± 2.2	2.3		20.0	88.7 ± 3.5	3.9		20.0	98.7 ± 3.1	3.1		20.0	90.2 ± 4.2	4.7	
		200.0	92.3 ± 3.7	4.0		200.0	96.5 ± 2.9	3.0		200.0	95.2 ± 2.7	2.8		200.0	86.3 ± 2.0	2.3		200.0	85.9 ± 4.0	4.7	
Pomelo tea	ND	5.0	84.8 ± 2.5	2.9	ND	5.0	89.1 ± 3.3	3.7	ND	5.0	92.4 ± 4.4	4.8	ND	5.0	92.0 ± 3.6	3.9	ND	5.0	87.7 ± 3.2	3.6	ND
		20.0	103.1 ± 4.7	4.6		20.0	87.5 ± 4.6	5.3		20.0	93.3 ± 2.9	3.1		20.0	87.8 ± 2.5	2.8		20.0	88.9 ± 1.7	1.9	
		200.0	93.5 ± 2.6	2.8		200.0	105.3 ± 3.1	2.9		200.0	90.6 ± 1.5	1.7		200.0	85.3 ± 2.2	2.6		200.0	94.3 ± 3.4	3.6	
Plum juice	ND	5.0	98.1 ± 3.4	3.5	ND	5.0	97.3 ± 2.4	2.5	ND	5.0	87.1 ± 2.8	3.2	ND	5.0	96.9 ± 1.8	1.9	ND	5.0	96.9 ± 1.8	1.9	ND
		20.0	90.6 ± 4.2	4.6		20.0	94.7 ± 3.8	4.0		20.0	85.9 ± 3.1	3.6		20.0	91.8 ± 3.7	4.0		20.0	82.4 ± 2.6	3.2	
		200.0	91.7 ± 2.4	2.6		200.0	84.2 ± 2.9	3.4		200.0	99.2 ± 4.2	4.2		200.0	101.2 ± 2.0	2.0		200.0	92.3 ± 4.6	5.0	
Orange juice	ND	5.0	85.8 ± 1.7	2.0	ND	5.0	82.7 ± 1.5	1.8	ND	5.0	87.4 ± 2.9	3.3	ND	5.0	94.5 ± 2.1	2.2	ND	5.0	92.6 ± 3.9	4.2	ND
		20.0	92.4 ± 3.9	4.2		20.0	99.3 ± 4.8	4.8		20.0	85.1 ± 1.0	1.2		20.0	87.3 ± 4.5	5.2		20.0	88.9 ± 4.1	4.6	
		200.0	101.3 ± 1.9	1.9		200.0	96.4 ± 4.1	4.3		200.0	92.1 ± 4.2	4.6		200.0	85.7 ± 2.9	3.4		200.0	83.2 ± 1.5	1.8	
Pear juice	ND	5.0	91.2 ± 2.2	2.4	ND	5.0	88.1 ± 2.7	3.1	ND	5.0	100.5 ± 3.7	3.7	ND	5.0	94.1 ± 4.0	4.3	ND	5.0	96.7 ± 3.6	3.7	ND
		20.0	83.9 ± 4.3	5.1		20.0	87.5 ± 4.2	4.8		20.0	93.5 ± 2.6	2.8		20.0	90.9 ± 3.9	4.3		20.0	88.0 ± 2.5	2.8	
		200.0	99.2 ± 1.4	1.4		200.0	93.3 ± 3.6	3.9		200.0	94.8 ± 1.7	1.8		200.0	98.2 ± 2.1	2.1		200.0	87.3 ± 1.4	1.6	
Lactobacillus	ND	5.0	85.3 ± 2.0	2.3	ND	5.0	89.0 ± 1.2	1.3	ND	5.0	94.6 ± 2.9	3.1	ND	5.0	96.5 ± 4.4	4.6	ND	5.0	94.8 ± 3.9	4.1	ND
		20.0	88.4 ± 1.2	1.4		20.0	90.8 ± 2.5	2.8		20.0	93.9 ± 3.1	3.3		20.0	98.1 ± 2.8	2.9		20.0	93.1 ± 3.6	3.9	
		200.0	93.2 ± 3.1	3.3		200.0	93.1 ± 3.3	3.5		200.0	102.4 ± 3.0	2.9		200.0	97.3 ± 3.4	3.5		200.0	95.1 ± 2.2	2.3	

Notes: ND indicates non-detectable or below detectable level. ERS denote extraction recoveries for six BPs. Each treatment was conducted in three replicates ( $n = 3$ ). The experimental conditions were as follows: (2) extraction process: 150 mg of TTA and 106 mg  $\text{Na}_2\text{CO}_3$  as precursors of an effervescent tablet, 7.4 mg of CoNi-N-CNTs/rGO as extractant,  $\text{pH} = 6.8$ , 1638  $\mu\text{L}$  of acetone as eluent solution and 6 min extraction time.

with increasing BP concentrations from 0 to 15 mg/L (Fig. 5a). In particular, the  $Q_e$  of BPM increased in a linear concentration-dependent manner. At an initial BPM concentration of 15 mg/L, the maximum  $Q_e$  for BPM reached 289.5 mg/g. The adsorption of BPA and BPM by CoNi-N-CNTs/rGO mainly occurred in the first 5 min at 298 K and reached up to 98.2% and 99.0%, respectively (Fig. 5b). Overall, the adsorption capacity increased rapidly in the first 10 min, and all six BPs reached apparent adsorption equilibrium at  $\sim 30$  min; adsorption of all six BPs were  $> 80\%$ , except for BPB (73.9%). Notably, sorption of BPZ, BPA, and BPM were nearly 100% (Fig. 5b).

To elucidate the underlying adsorption mechanisms, the CoNi-N-CNTs/rGO nanocomposite before and after adsorption was analyzed by FT-IR spectroscopy (Fig. 5c). Pre-sorption, the absorption peak at 3400–3600  $\text{cm}^{-1}$  indicates the presence of –OH in the as-synthesized bimetallic carbon nanocomposite. Post-sorption, the –OH absorption peak shifted from 3440 to 3438  $\text{cm}^{-1}$ , suggesting that –OH was involved in adsorption at H-bonding sites [39]. The characteristic peak at  $\sim 2900$   $\text{cm}^{-1}$  was attributable to aromatic C–H stretching vibration, and the aromatic C = C skeleton vibration band appearing at  $\sim 1590$   $\text{cm}^{-1}$  provides evidence for the existence of graphite. The peak shift ( $\sim 10$   $\text{cm}^{-1}$ ) for C = C after BP adsorption implies that  $\pi$ - $\pi$  conjugation played an important role in the adsorption process [40]. The characteristic peaks for C–N and C–O bonds at  $\sim 1270$   $\text{cm}^{-1}$  not only demonstrated the successful doping of N, but also the presence of abundant oxygen-containing functional groups, which were conducive to BP adsorption on the CoNi-N-CNTs/rGO surface. Moreover, a small shift in the C–N and C–O bonds was observed from the stretching vibration at 1263 to 1270  $\text{cm}^{-1}$ , which possibly resulted from hydrogen bonding effects [47]. The characteristic peaks at 700  $\sim$  900  $\text{cm}^{-1}$  were attributable to the bending vibration of C–H and the plane oscillation of  $\delta\text{CH}_2$ . Furthermore, the peak at 550  $\text{cm}^{-1}$  may result from the characteristic vibration owing to excitation of rGO by the Co–Ni alloy [41].

The IR spectra shifts between pre- and post-BP sorption infer that hydrogen bonding and  $\pi$ - $\pi$  conjugation were active in the adsorption of BPs by the nanocomposites, as shown in Fig. 5d, the hydrophobic interactions in the solution system where the CoNi-N-CNTs/rGO material adsorption/extraction BPs reaction takes place needs to be considered. N-doping was conducive to the enhancement of all three bonding mechanisms for BP adsorption, which is consistent with previous reports [28–33]. However, different N-doping strategies have various effects on the adsorption of target molecules.

To unravel the effects of different N-doping types and explore the energetics of BP adsorption sites on the nanocomposite surface, DFT theoretical simulation calculations were conducted. The rGO model was used to simulate the carbon structure in nanocomposites. As described above, the nanocomposites had a maximum equilibrium adsorption capacity and extraction efficiency for BPM. Hence, adsorption processes for BPM molecules at pyrrolic-N, pyridinic-N, and graphitic-N sites were investigated in detail as informed by XPS analyses. By using BPM as a model molecule, the H-bonding force, hydrophobic interactions and  $\pi$ - $\pi$  conjugation were assessed, and the adsorption energy ( $\Delta E_a$ ) among molecules was computed (Fig. 6). Within a given N-doping type,  $\pi$ - $\pi$  conjugation had the greatest influence on adsorption. These prediction based on molecular theory infer that  $\pi$ - $\pi$  conjugation plays an important role in promoting the adsorption of aromatic compounds on carbon materials, and the defect sites are conducive to enhancement of adsorption performance [33,35]. Previous mechanistic analyses confirmed that pyridinic-N activity was higher than that of graphitic-N and pyrrolic-N for BPA adsorption. The pyridinic-N adsorption energy was higher than those of other sites, and this site had a stronger affinity for BPA [32,33]. The adsorption energies ( $\Delta E_a$ ) among graphitized-N, pyridinic-N, and pyrrolic-N with BPM molecules were  $-1.80$ ,  $-1.59$ , and  $-2.08$  eV, demonstrating that sorption was most energetically favorable at pyrrolic-N sites. H-bonding and hydrophobicity are also facilitated by the presence of graphitized N. Based on XPS characterization of N1s in the nanocomposites, the total N-doping percentage in

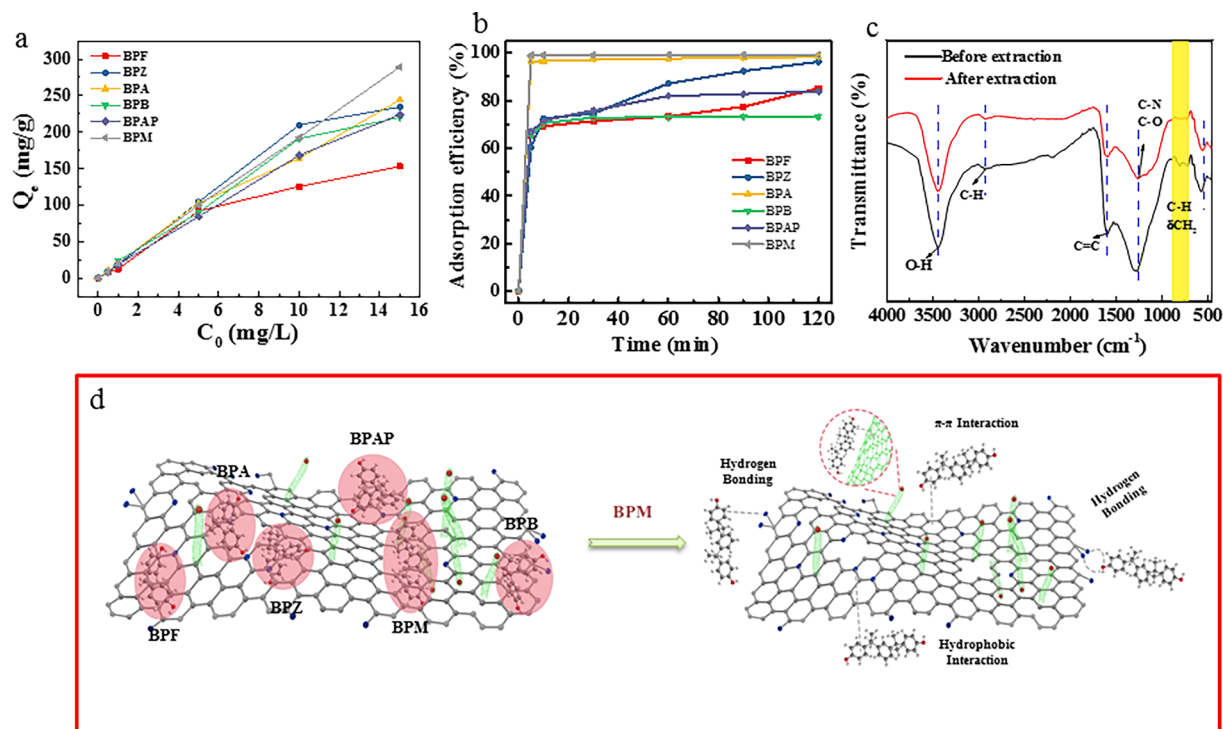


Fig. 5. (a) Adsorption isotherms and (b) effect of contact time on adsorption efficiency of BPs; (c) changes in the FT-IR spectrum of CoNi-N-CNTs/rGO before and after adsorption of BPs; and (d) schematic illustration of adsorption mechanisms for BPs on CoNi-N-CNTs/rGO.

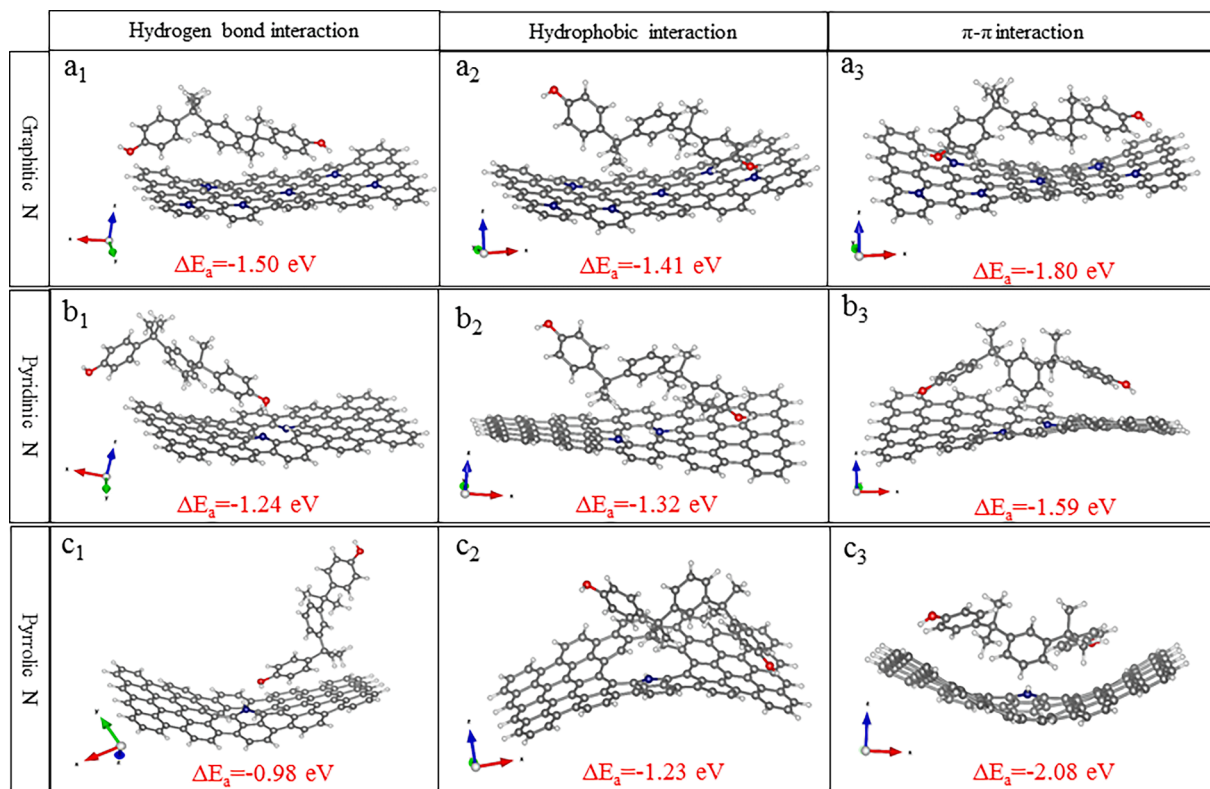


Fig. 6. Adsorption energies ( $\Delta E_a$ ) for the three interaction forces between CoNi-N-CNTs/rGO and BPM molecule:  $a_1, a_2, a_3$ : Graphitic N;  $b_1, b_2, b_3$ : Pyridinic N;  $c_1, c_2, c_3$ : Pyrrolic N and  $a_1, b_1, c_1$ : Hydrogen bond interaction;  $a_2, b_2, c_2$ : Hydrophobic interaction;  $a_3, b_3, c_3$ :  $\pi-\pi$  interaction.

the nanomaterial was  $\sim 7.98\%$ , for which the pyrrolic-N, graphitized-N, and pyridinic-N sites accounted for 31.5, 9.7, and 37.4%, respectively. As detailed in Fig. S5, following BPM adsorption, the percentage of

pyrrolic-N decreased to 15.5%, whereas graphitized-N and pyridinic-N increased to 16.0% and 40.3%, respectively. These data offer compelling evidence that BPM molecules have the strongest affinity for

Table 5

Comparison of the ET-MSPE/HPLC-FLD method with other common methods for the determination of bisphenols in juice samples.

Extraction mode	Adsorbent/ Extractant	Analytes	Dosage	Extraction time	Analytical technique	Linear range ( $\mu\text{g L}^{-1}$ )	LODs	Recovery (%)	References
TIWIM	[C <sub>4</sub> MIM-SH]Br	BPA, BPB, BPAF	60 $\mu\text{L}$	15 min	HPLC-FLD	0.5–500	0.13–0.82 $\mu\text{g/L}$	91.6–107.9	9
MSPE	Fe <sub>3</sub> O <sub>4</sub> @MgAl LDHs NPs	BPA, BPAF, TBBPA	5.8 mg	15 min	HPLC-UV	5–1000	0.37–0.63 $\mu\text{g/L}$	84–103	26
MSPE	3D-G iron oxide	BPA	20 mg	20 min	HPLC-FLD	0.5–100	0.010–0.025 $\mu\text{g/L}$	88.8–108.8	42
SPE	MOF-5-C	BPA	15 mg	–	HPLC-UV	0.15–100	0.04 $\mu\text{g/L}$	89–97	43
MSPE	M–N–CNTs	BPA, BPB, BPAF, TBBPA	5.76 mg	10.22 min	HPLC-MS	0.002–1.0	0.43–2.47 ng/L	90.6–101	44
MSPE	Fe <sub>3</sub> O <sub>4</sub> @MON-NH <sub>2</sub>	BPA	4 mg	40 min	HPLC-UV	0.05–1000	0.015–0.03 $\mu\text{g/L}$	81–107.4	45
MSPE	CoNi-N-CNTs/rGO	BPA, BPB, BPM, BPAF, BPZ, BPAP	7.4 mg	6 min	HPLC-FLD	0.33–500	0.06–0.20 $\mu\text{g/L}$	82.4–103.7	This work

**Note:** TIWIM: thiol imidazolium-based ionic liquid for ultrasonic assisted liquid–liquid microextraction; MSPE: magnetic solid-phase extraction; SPE: solid-phase extraction.

pyrrolic-N sites during the adsorption process [32]. Based upon the above analyses, we posit that  $\pi$ - $\pi$  interactions had the largest contribution to BP adsorption among the three interaction forces evaluated for BP adsorption by CoNi-N-CNTs/rGO nanocomposites. Importantly, N doping supplies an abundance of active sites for BP adsorption, for which pyrrolic-N displays the strongest affinity for BPM molecules.

### 3.2.8. Performance of the newly developed method compared to conventional techniques

In the ET-MSPE/HPLC-FLD method, the magnetic nanocomposites, with 3D structure, abundant pores and N doping, provide the basis for adsorption/extraction of trace-level BPs. Incorporating an effervescent reaction enhanced dispersion and extraction efficiency, while the strongly magnetic Co-Ni alloy facilitated separation of the nanomaterials from the aqueous phase. Based on a series of performance metrics, the newly developed method demonstrated great efficacy for trace-level BP determination in fruit juices. Distinct advantages of the new method include: (1) multiple BPs can be adsorbed/extracted simultaneously [9,26,42–45]; (2) extraction time is much shorter (~6 min) than previous methods that take an average of 10–20 min [9,26,42–44] and as long as 40 min [45]; and (3) compared to MSPE-UHPLC-MS, the new method provides comparable LODs (0.06–0.20  $\mu\text{g/L}$ ) and recoveries (82.4–103.7%) while achieving easy to perform pretreatment [44]. We summarize several performance metrics of the ET-MSPE/HPLC-FLD method compared with other conventional methods for BP determination of juice samples in Table 5. Overall, the newly developed methodology offers a low adsorbent/extractant dosage requirement, short extraction time, and simultaneous detection of multiple bisphenolic pollutants. In terms of analytical performance, the new method provides lower LODs, higher ERs, and a wider LR compared to other solid-phase or liquid–liquid microextraction methodologies. Consequently, the ET-MSPE/HPLC-FLD method offers a promising alternative approach for routine monitoring of trace-level BPs in food matrices.

## 4. Conclusions

A 3D CoNi-N-CNTs/rGO nanocomposite was fabricated by facile calcination for use as an adsorbent/extractant in the ET/MSPE procedure. This nanomaterial has excellent magnetic properties, and is easy to separate from the aqueous phase with the use of an external magnet. N-doping of the nanocomposite increased the number of defect sites and effectively enhanced  $\pi$ - $\pi$  conjugation between BPs molecules and the nanocomposite, thereby improving the adsorption/extraction performance. By combining the nanocomposites with acidic and alkaline

sources into an effervescent tablet, the ET/MSPE/HPLC-FLD approach was developed for the simultaneous determination of several BPs in fruit juice samples. This newly developed method integrated highly efficient adsorption/extraction and rapid dispersion into one synchronous step, thereby achieving a wider LR, lower LODs and good ERs for detection of several BPs using a simple and inexpensive operation when compared to conventional microextraction procedures. Overall, the newly developed ET/MSPE/HPLC-FLD method demonstrated strong efficacy for applications in trace-level BP monitoring and for removal of BPs from environmental and food matrices.

## Declaration of Competing Interest

The authors declare that they have no known competing financial interests or personal relationships that could have appeared to influence the work reported in this paper.

## Data availability

No data was used for the research described in the article.

## Acknowledgements

This work was jointly sponsored by the Natural Science Foundation of China (21876125, 22076134), Jiangsu Provincial Natural Science Foundation (BK20211338), Key Science & Technology Project of Suzhou City (SS202028), and Jiangsu Provincial Key R&D Project (SBE2022740011).

## Appendix A. Supplementary data

Supplementary data to this article can be found online at <https://doi.org/10.1016/j.cej.2022.137690>.

## References

- [1] A.M. Soto, C. Sonnenschein, Environmental causes of cancer: endocrine disruptors as carcinogens, *Nat Rev Endocrinol.* 6 (7) (2010) 363–370.
- [2] K. Khan, K. Roy, E. Benfenati, Ecotoxicological QSAR modeling of endocrine disruptor chemicals, *J Hazard Mater.* 369 (2019) 707–718.
- [3] M.-Y. Chen, M. Ike, M. Fujita, Acute toxicity, mutagenicity, and estrogenicity of bisphenol A and other bisphenols, *Environ Toxicol.* 17 (1) (2002) 80–86.
- [4] J.F. Yin, Z.H. Meng, Y.S. Zhu, M.Y. Song, H.L. Wang, Dummy molecularly imprinted polymer for selective screening of trace bisphenols in river, *Anal Meth.* 3 (2011) 173–180.
- [5] L. Lian, X. Jiang, J. Guan, Z. Qiu, X. Wang, D. Lou, Dispersive solid-phase extraction of bisphenols migrated from plastic food packaging materials with cetyltrimethylammonium bromide-intercalated zinc oxide, *J Chromatogr A.* 1612 (2020) 460666.

- [6] W.H. Qiu, H.Y. Zhan, J.Q. Hu, T. Zhang, H. Xu, M.H. Wong, B.T. Xu, C.M. Zheng, The occurrence, potential toxicity, and toxicity mechanism of bisphenol S, a substitute of bisphenol A: a critical review of recent progress, *Ecotoxicol Environ Saf.* 173 (2019) 192–202.
- [7] S. Han, Y. Song, J. Hu, R. Liu, Y. Chi, A.n. Kang, H. Deng, D. Zhu, Novel computer-assisted separation prediction strategy for online-enrichment-HPLC-FLD in simultaneous monitoring of bisphenols in children's water bottles, *Food Chem.* 339 (2021) 127766.
- [8] W. Ding, X. Wang, T. Liu, M. Gao, F. Qian, H. Gu, Z. Zhang, Preconcentration/extraction of trace bisphenols in milks using a novel effervescent reaction-assisted dispersive solid-phase extraction based on magnetic nickel-based N-doped graphene tubes, *Microchem J.* 150 (2019) 104109.
- [9] J.G. Qu, Y.Y. Li, M. Gao, C.X. Tan, J.Y. Li, X.D. Wang, H.L. Wang, Development and optimization of a thiol imidazolium-based ionic liquid for ultrasonic assisted liquid-liquid microextraction combined with HPLC-FLD for determination of bisphenols in milk and juice samples, *LWT.* 111 (2019) 653–662.
- [10] A. Kaleniecka, P.K. Zarzycki, Analysis of selected endocrine disrupters fraction including bisphenols extracted from daily products, food packaging and treated wastewater using optimized solid-phase extraction and temperature-dependent inclusion chromatography, *Molecules* 24 (2019) 1285.
- [11] M. Mahdavianpour, N. Chamkouri, H. Chamkouri, Z. Kolivand, N. Noorzadeh, S. M.A. Malaekheh, S. Karami, Determination of bisphenol A migration from food packaging by dispersive liquid-liquid microextraction, *Methods X.* 8 (2021) 101415.
- [12] T. Liu, E. AgyeKum, S. Ma, H. Ye, J. Li, M. Gao, M. Ni, X. Zhang, X. Wang, Novel nanohybrids for effervescence enhanced magnetic solid-phase microextraction of wide-polarity organic pollutants in roasted meat samples, *J Sep Sci.* 44 (24) (2021) 4313–4326.
- [13] G. Lasarte-Aragones, R. Lucena, S. Cardenas, M. Valcarcel, Effervescence assisted dispersive liquid-liquid microextraction with extractant removal by magnetic nanoparticles, *Anal Chim Acta.* 807 (2014) 61–66.
- [14] X.L. Yang, P.J. Zhang, X.B. Li, L. Hu, H.X. Gao, S.B. Zhang, W.F. Zhou, R. Lu, Effervescence-assisted beta-cyclodextrin/attapulgite composite for the in-syringe dispersive solid-phase extraction of pyrethroids in environmental water samples, *Talanta* 153 (2016) 353–359.
- [15] P.P. Zhou, K. Chen, M. Gao, J.G. Qu, Z.E. Zhang, R.A. Dahlgren, Y.Y. Li, W. Liu, H. Huang, X.D. Wang, Magnetic effervescent tablets containing ionic liquids as a non-conventional extraction and dispersive agent for determination of pyrethroids in milk, *Food Chem.* 268 (2018) 468–475.
- [16] W. Zhang, P. Zhou, W. Liu, H. Wang, X. Wang, Enhanced adsorption/extraction of five typical polycyclic aromatic hydrocarbons from meat samples using magnetic effervescent tablets composed of dicationic ionic liquids and NiFe<sub>2</sub>O<sub>4</sub> nanoparticles, *J Mol Liq.* 315 (2020) 113682.
- [17] P. Zhou, R. Wang, R.u. Fan, X. Yang, H.e. Mei, H. Chen, H. Wang, Z. Wang, X. Wang, Magnetic amino-functionalized metal-organic frameworks as a novel solid support in ionic liquids-based effervescent tablets for efficient extraction of polycyclic aromatic hydrocarbons in milks, *Ecotoxicol Environ Saf.* 222 (2021) 112482.
- [18] J.A. Naser, Z.W. Ahmed, E.H. Ali, Nanomaterials usage as adsorbents for the pollutants removal from wastewater: a review, *Mat Today: Proc.* 42 (2021) 2590–2595.
- [19] S.-H. Rajabnejad, H.B. Bostan, A. Verdian, G.R. Karimi, E. Fooladi, J. Fyzi, Aptasensors as promising new tools in bisphenol A detection - an invisible pollution in food and environment, *Microchem J.* 155 (2020) 198–205.
- [20] Z. Peng, X. Liu, W. Zhang, Z. Zeng, Z. Liu, C. Zhang, Y. Liu, B. Shao, Q. Liang, W. Tang, X. Yuan, Advances in the application, toxicity and degradation of carbon nanomaterials in environment: a review, *Environ Int.* 134 (2020) 105298.
- [21] S. Wan, O. Xu, X. Zhu, Synthesis of ionic liquid modified metal-organic framework composites and its application in solid-phase extraction: a review, *Ionics* 27 (2) (2021) 445–456.
- [22] C. Tan, J. Li, W. Liu, Q. Zhao, X. Wang, Y. Li, Core-shell magnetic covalent organic framework nanocomposites as an adsorbent for effervescent reaction-enhanced microextraction of endocrine disruptors in liquid matrices, *Chem Eng J.* 396 (2020) 125191.
- [23] S. Bhogal, K. Kaur, I. Mohiuddin, S. Kumar, J. Lee, R.J.C. Brown, K.-H. Kim, A. K. Malik, Hollow porous molecularly imprinted polymers as emerging adsorbents, *Environ Pollut.* 288 (2021) 117775.
- [24] G. Yu, Y. Lu, J. Guo, M. Patel, A. Bafana, X. Wang, B. Qiu, C. Jeffries, S. Wei, Z. Guo, E.K. Wujcik, Carbon nanotubes, graphene, and their derivatives for heavy metal removal, *Adv Compos Hybrid Mater.* 1 (1) (2018) 56–78.
- [25] H. Sun, Z. Xu, C. Gao, Multifunctional, ultra-flyweight, synergistically assembled carbon aerogels, *Adv Mater.* 25 (18) (2013) 2554–2560.
- [26] L.i. Liu, T. Feng, C. Wang, Q. Wu, Z. Wang, Magnetic three-dimensional graphene nanoparticles for the preconcentration of endocrine-disrupting phenols, *Microchim Acta.* 181 (11–12) (2014) 1249–1255.
- [27] Y. Shen, X.Y. Zhu, L.Z. Zhu, B.L. Chen, Synergistic effects of 2D graphene oxide nanosheets and 1D carbon nanotubes in the constructed 3D carbon aerogel for high performance pollutant removal, *Chem Eng J.* 314 (2017) 336–346.
- [28] T. Wang, Z. Cheng, Y. Liu, W. Tang, T. Fang, B. Xing, Mechanistic understanding of highly selective adsorption of bisphenols on microporous-dominated nitrogen-doped framework carbon, *Sci Total Environ.* 762 (2021) 143115.
- [29] W. Zhang, M. Yang, H. Zhang, X. Yu, W. Zhang, A.T.S. Wee, X. Yan, J. Qi, J. Li, A confinement approach to fabricate hybrid PBAs-derived FeCo@NC yolk-shell nanoreactors for bisphenol A degradation, *Chem, Eng J.* 428 (2022) 131080.
- [30] X. Wang, Y. Qin, L. Zhu, H. Tang, Nitrogen-doped reduced graphene oxide as a bifunctional material for removing bisphenols: synergistic effect between adsorption and catalysis, *Environ Sci Technol.* 49 (11) (2015) 6855–6864.
- [31] S. Cai, Q. Zhang, Z.Q. Wang, S. Hua, D.H. Ding, T.M. Cai, R.H. Zhang, Pyrolytic N-rich biochar without exogenous nitrogen doping as a functional material for bisphenol A removal: performance and mechanism, *Appl Catal B: Environ.* 291 (2021), 120093.
- [32] W. Wang, X. Wang, J. Xing, Q. Gong, H. Wang, J. Wang, Z. Chen, Y. Ai, X. Wang, Multi-heteroatom doped graphene-like carbon nanospheres with 3D inverse opal structure: a promising bisphenol-A remediation material, *Environ Sci: Nano.* 6 (3) (2019) 809–819.
- [33] L. Yi, L. Zuo, C. Wei, H. Fu, X. Qu, S. Zheng, Z. Xu, Y. Guo, H. Li, D. Zhu, Enhanced adsorption of bisphenol A, tylosin, and tetracycline from aqueous solution to nitrogen-doped multiwall carbon nanotubes via cation- $\pi$  and  $\pi$ - $\pi$  electron-donor-acceptor (EDA) interactions, *Sci Total Environ.* 719 (2020) 137389.
- [34] N. Li, J. Chen, Y.P. Shi, Magnetic nitrogen-doped reduced graphene oxide as a novel magnetic solid-phase extraction adsorbent for the separation of bisphenol endocrine disruptors in carbonated beverages, *Talanta* 201 (2019) 194–203.
- [35] Z. Li, X. Zhao, X. Hong, H. Yang, D. Fang, Y. Wang, M. Lei, Green synthesis and optimization of 3D nitrogen-doped carbon network via biomass waste for highly efficient bisphenol S adsorption, *ChemistrySelect* 6 (25) (2021) 6348–6352.
- [36] L. Du, X. Wang, T. Liu, J. Li, J. Wang, M. Gao, H. Wang, Magnetic solid-phase extraction of organophosphorus pesticides from fruit juices using NiFe<sub>2</sub>O<sub>4</sub>@polydopamine@Mg/Al-layered double hydroxides nanocomposites as an adsorbent, *Microchem J.* 150 (2019) 104128.
- [37] X. Zhang, X. Zhang, H. Yuan, K. Li, Q. Ouyang, C. Zhu, S. Zhang, Y. Chen, CoNi nanoparticles encapsulated by nitrogen-doped carbon nanotube arrays on reduced graphene oxide sheets for electromagnetic wave absorption, *Chem Eng J.* 383 (2020) 123208.
- [38] C.Y. Su, H. Cheng, W. Li, Z.Q. Liu, N. Li, Z.F. Hou, F.Q. Bai, H.X. Zhang, T.Y. Ma, Atomic modulation of FeCo-nitrogen-carbon bifunctional oxygen electrodes for rechargeable and flexible all solid-state zinc air battery, *Adv Energy Mater.* 7 (2017) 67–75.
- [39] G. Lei, X. Hu, Z. Peng, J. Hu, H. Liu, Facile synthesis of reduced graphene oxide-modified, nitrogen-doped carbon xerogel with enhanced electrochemical capacitance, *Mater Chem Phys.* 148 (3) (2014) 1171–1177.
- [40] Z. Lin, G. Waller, Y. Liu, M. Liu, C.-P. Wong, Facile synthesis of nitrogen-doped graphene via pyrolysis of graphene oxide and urea, and its electrocatalytic activity toward the oxygen-reduction reaction, *Adv Energy Mater.* 2 (7) (2012) 884–888.
- [41] X. Yang, J.X. Li, T. Wen, X.M. Ren, Y.S. Huang, X.K. Wang, Adsorption of naphthalene and its derivatives on magnetic graphene composites and the mechanism investigation, *Colloid Surface A.* 422 (2013) 118–125.
- [42] D.Z. Yang, X.L. Li, D.L. Meng, M. Wang, Y.L. Yang, Supramolecular solvents combined with layered double hydroxide-coated magnetic nanoparticles for extraction of bisphenols and 4-tert-octylphenol from fruit juices, *Food Chem.* 237 (2017) 870–876.
- [43] J. Wang, L. Hao, C. Wang, Q. Wu, Z. Wang, Nanoporous carbon as the solid-phase extraction adsorbent for the extraction of endocrine disrupting chemicals from juice samples, *Food Anal Meth.* 10 (8) (2017) 2710–2717.
- [44] H.L. Jiang, Y.L. Lin, N. Li, Z.W. Wang, M. Liu, R.S. Zhao, J.M. Lin, Application of magnetic N-doped carbon nanotubes in solid-phase extraction of trace bisphenols from fruit juices, *Food Chem.* 269 (2018) 413–418.
- [45] Z.-D. Du, Y.-Y. Cui, C.-X. Yang, X.-P. Yan, Synthesis of magnetic amino-functionalized microporous organic network composites for magnetic solid phase extraction of endocrine disrupting chemicals from water, beverage bottle and juice samples, *Talanta* 206 (2020) 120179.
- [46] L. Hao, C. Wang, Q.H. Wu, Z. Li, X.H. Zang, Z. Wang, Metal-organic framework derived magnetic nanoporous carbon: novel adsorbent for magnetic solid-phase extraction, *Anal Chem.* 86 (24) (2014) 12199–12205.
- [47] Z.G. Pei, L.Y. Li, L.X. Sun, S.Z. Zhang, X.Q. Shan, S. Yang, B. Wen, Adsorption characteristics of 1,2,4-trichlorobenzene, 2,4,6-trichlorophenol, 2-naphthol and naphthalene on graphene and graphene oxide, *Carbon.* 51 (2013) 156–163.